

General Circulation of Antarctic Intermediate Water  
in the subtropical South Atlantic

Ismael Núñez-Riboni <sup>1,\*</sup>, Olaf Boebel <sup>1</sup>, Michel Ollitrault <sup>2</sup>,  
Yuzhu You <sup>3</sup>, Phil Richardson <sup>4</sup>, Russ Davis <sup>5</sup>

<sup>1</sup> Alfred Wegener Institute for Polar and Marine Research (AWI)  
Bussestraße 24, 27570 Bremerhaven, Germany.

<sup>2</sup> Institut Français de Recherche pour l'Exploitation de la Mer (IFREMER),  
Centre de Brest,  
BP 70, 29280 Plouzane, France.

<sup>3</sup> The University of Sydney Institute of Marine Science (USIMS)  
Edgeworth David Building F05, University of Sydney, NSW 2006, Australia.

<sup>4</sup> Woods Hole Oceanographic Institution (WHOI), Woods Hole, Massachusetts, 02543  
USA.

<sup>5</sup> Scripps Institution of Oceanography (SIO), UCSD  
9500 Gilman Drive  
La Jolla CA, 92093-0230  
Mail Code: 0230

\* Corresponding Author: Telephone: +49(471)4831-1877; Fax: +49(471)4831-1797;  
e-mail: [inunez@awi-bremerhaven.de](mailto:inunez@awi-bremerhaven.de)

## Abstract

This study combines float data from different projects collected between 1991 and 2003 in the South Atlantic to describe the flow of Antarctic Intermediate Water (AAIW). Velocity space-time averages are calculated for various grid resolutions and with cells deformed to match the bathymetry,  $f/H$  or  $f/h$  (with  $H$  being the water depth and  $h$  being the thickness of the AAIW layer). When judged by the degree of alignment between respective isolines and the resulting average velocity fields, the best grid is based on a nominal cell size of  $3^\circ$  (latitude) by  $4^\circ$  (longitude) with cell shapes deformed according to  $f/h$ . Using this grid, objectively estimated mean currents (and their associated errors), as well as meridional and zonal volume transports are estimated. Results show an anticyclonic Subtropical Gyre centred near  $36^\circ\text{S}$  and spanning from  $23^\circ \pm 1^\circ\text{S}$  to  $46^\circ \pm 1^\circ\text{S}$ . The South Atlantic Current meanders from  $33^\circ\text{S}$  to  $46^\circ\text{S}$  and shows a mean speed of  $9.6 \pm 7.8 \text{ cm s}^{-1}$  ( $13 \text{ Sv} \pm 3 \text{ Sv}$ ). The northern branch of the Subtropical Gyre is located between  $22^\circ\text{S}$  and  $32^\circ\text{S}$  and flows westward with a mean speed of  $4.7 \pm 3.3 \text{ cm s}^{-1}$  ( $12 \text{ Sv} \pm 2 \text{ Sv}$ ). Evidence of a cyclonic Tropical Gyre divided in two subcells by the Midatlantic Ridge is visible on the stream function. Comparisons with transport values found in the literature are discussed.

**Keywords:** Antarctic Intermediate Water (AAIW), floats, neutral density surfaces, South Atlantic, general circulation, transports, objective analysis.

## Introduction

During the late 20's of the last century, Deacon (1933) and Wüst (1935) first recognized Antarctic Intermediate Water (AAIW) throughout the South Atlantic by virtue of its mid-depth vertical salinity minimum (see Appendix). Since then, the presence of AAIW has been documented in all three world oceans, with its freshest variety ( $S \approx 34.2$ ) observable in the South

Atlantic, directly to the north of the Subtropical Convergence where the salinity minimum outcrops. Throughout the subtropical South Atlantic, AAIW occupies the depth range from 650 to 1050 meters (Reid, 1994), with typical temperature and salinity values of 3°C and 34.3, respectively (Tomczak and Godfrey, 1994). AAIW spreads across the equator and traces thereof  
5 can be found as far north as 30°N in the North Atlantic (Talley, 1996; Figure 1 below). In the Indian Ocean, AAIW reaches the Bay of Bengal (You, 1998), whereas in the Pacific it does not extend past the equator (Tomczak and Godfrey, 1994).

In the subtropical South Atlantic, based on hydrographic measurements, Deacon (1933) and Wüst (1935) suggested a basin wide, sluggish northward flow of AAIW, with Wüst (1935) in  
10 addition proposing a slightly intensified flow along the Brazilian shelf for latitudes lower than 20°S. Subsequent geostrophic calculations (Defant, 1941) suggested a continuous northward intermediate western boundary current from 30°S to the equator and beyond, while retaining significant interior northward currents for the region south of 25°S. More recently, estimates based on the geostrophic method (Reid, 1989; Gordon and Bosley, 1991; Suga and Talley, 1995;  
15 Talley, 1996), replaced this concept of a basin wide northward flow by a succession of two basin scale, zonally stretched gyres: the anticyclonic Subtropical Gyre centred along 34°S and the cyclonic Tropical Gyre (Gordon and Bosley, 1991) centred at about 10-15°S (See Figure 2). Further refinements within these gyres have been suggested by Suga and Talley (1995). They argue that three smaller gyres reside inside the Tropical Gyre (Suga and Talley call it  
20 Subequatorial Gyre): two cyclonic cells at the northern and southern limits of the gyre, and an anticyclonic cell between them (centred at about 13°S). However, the appropriateness of the concepts of a Tropical Gyre as such and of nested multi-gyres within remain obscure. Similarly, the strengths of the gyres interactions, either during the waters cross-basin advection or when encountering ocean margins, are poorly known. These shortcomings are primarily based on the

general scarceness of data in the South Atlantic and the resulting questionable representativeness of single hydrographic sections, as well as on the familiar problems of choosing the correct reference layer for geostrophic analyses.

Recent technological advances have enabled us to obtain direct velocity measurements not only at selected sites, but over vast oceanic regions of the South Atlantic, using neutrally buoyant, freely drifting floats (Rossby et al., 1986; Davis et al., 1996). The combination of these direct and geostrophic current measurements resulted in the following flow pattern: The current resulting from the merging of the Malvinas and the Brazil currents in the Confluence Zone (the South Atlantic Current, Stramma and Peterson, 1990) crosses the South Atlantic basin until it interacts with waters from the Indian Ocean in the Cape Basin Agulhas System. The resulting melange forms the wider Benguela Current (Stramma and Peterson, 1989; Richardson and Garzoli, 2003). This deep expression of the Benguela Current eventually turns westwards (where sometimes it is called Benguela Current Extension, Richardson and Garzoli, 2003) and forms the northern branch of the Subtropical Gyre.

Flowing across the Walvis and Mid-Atlantic Ridge, it finally reaches the South American coast where it splits in two branches at the Santos Bifurcation (Boebel, et al., 1999a). One branch is a narrow northward intermediate western boundary current (IWBC) (counter to the northern Brazil Current flowing southward near the surface), carrying AAIW to the tropics and eventually to the equatorial region. There, a series of alternating jets are hypothesised to facilitate the cross-equatorial transfer between 5°S and 5°N (Boebel et al., 1999a and c; Schmid et al., 2001; Molinari, 1981; Reid, 1996; Talley, 1996, Ollitrault, 1994a, 1999; Richardson and Schmitz, 1993; Jochum and Manalotte-Rizzoli, 2003). The other branch deriving from the Santos Bifurcation is a south-westward flowing current forming a deep extension of the southern Brazil Current, ultimately closing the circuit of the Subtropical Gyre. This limb would carry recirculated AAIW

into the Confluence Zone, where it would be mixed with freshly formed AAIW from the Subantarctic Front, resulting in waters thought to become entrained into the Subtropical Gyre once more (Boebel et al., 1999b).

The main goal of the study at hand is to provide a comprehensive analysis of the motion of AAIW throughout the entire subtropical South Atlantic as based on Lagrangian direct velocity measurements. To this end we collected float data from historic and contemporary Lagrangian programs, compiling South Atlantic float data from more than a decade. From this data set, we computed space-time averages and objectively mapped velocity and mean kinetic energy fields as well as volume transports for the AAIW layer. Previous Lagrangian studies (e.g. Davis, 1996, Boebel et al., 1999b) chose the details of spatial grid subjectively. To obtain the optimum balance between spatial resolution and statistical robustness, however, the choice of an adequate spatial grid is of a vital importance: a coarse resolution yields currents structures that lack of spatial resolution while a resolution too fine may yield average currents contaminated with mesoscale processes.

An extreme illustration of the first situation would be the hypothetical merging of opposing currents through an unfortunate grid choice, leading to their mutual cancellation, while in the second situation a single transient eddy could result become interpreted as permanent recirculation cell. Here we propose an objective method to choose a “best” spatial averaging grid. These calculations are succeeded by objective mapping (OM) of the resulting averaged velocities using selected “best” OM parameters, i.e. the error of the climatological field and the space correlation length.

Finally, the selection of vertical boundaries of the AAIW layer by potential density or isobaric surfaces, as executed in previous studies, directly influences the soundness of these results. Potential density is a poor proxy of the vertical structure of the AAIW layer, especially

when only a single isopycnal surface is used, while isobaric surfaces aggravate this problem further. Therefore we constrained the AAIW layer by neutral density surfaces, which aptly approximate the vertical structure of the layer (You, 2002; You et al., 2003). However, for comparison, we also estimate and discuss the flow field as constrained by isobaric surfaces.

5

### **Data description**

This study is based on two types of data: float trajectory data and hydrographic data. The first provided us with direct Lagrangian current measurements in the intermediate depth layer. The latter was used to construct neutral density surfaces for the AAIW layer core and its upper and lower boundaries, in order to select the float's data in the vertical. This hydrographic data was also used to calculate geostrophic shear within the AAIW layer, to project the float velocities onto the central neutral surface.

#### ***Float Data***

Floats are neutrally buoyant buoys that drift freely at depth. Consequently, even weak oceanic subsurface currents are captured by the floats' paths (see article by John Gould, this volume). Float trajectories can be established by either recording satellite positional fixes when floats surface at pre-programmed intervals (ALACE and APEX floats, Davis et al., 1992) or via triangulation of sound signal arrival times (SOFAR floats, Rossby and Webb, 1970; RAFOS floats, Rossby et al., 1986; MARVOR floats, Ollitrault et al., 1994b).<sup>1</sup> While position is determined once or twice daily for acoustically tracked floats, pop-up float positions are determined at intervals ranging from one to two weeks. With pop-up floats rising to the surface for positioning, individual float displacements can and must be considered statistically independent, as unknown geostrophic current shear and Ekman currents generate a decorrelation

---

<sup>1</sup> Floats located through satellites fixes must ascend periodically to the surface to transmit their data, which is why there are frequently called pop-up floats.

between ascent and descent positions. Hence, the “trajectory” of a pop-up float is by itself of little relevance, and is named hereinafter “sequence of displacements”. Acoustically tracked floats, by contrast, continuously follow their surrounding water parcel and, hence, their trajectories are meaningful in a quasi-Lagrangian sense (Rossby et al., 1985).

5           We have selected float data inside the region bounded by the 4°S and 70°S parallels and by the 70°W and 30°E meridians (Figure 3). Floats with parts of their trajectory inside this box are included in the float count by float projects given below. However, for the number of float-years, as well as for the final data set used in the analysis, only those float displacements found inside the above region are considered. The float trajectory data set (Figure 3 and Table 1) 10 comprises 451 float years including 38 APEX floats from Alfred Wegener Institute (AWI), 19 of which co-join the Argo project, 60 APEX floats from the Argo project (in addition to the 19 AWI floats), 42 ALACE and P-ALACE floats from the WOCE (World Ocean Circulation Experiment) and CORC (Consortium on the Ocean’s Role in Climate) programmes, 101 RAFOS floats of the 15 KAPEX (Cape of Good Hope Experiment), 74 MARVOR floats from the SAMBA (SubAntarctic Motions in the Brazil Basin) experiment, including all SAMBA1 and SAMBA2 data and 71 RAFOS floats from the WOCE/DBE.

Most of the pop-up floats cycled every 10 days, except for some AWI floats, which cycled every 7 days. Occasionally, subsurface displacements lasted longer than 10 days, which might have been due to either poor satellites fixes preventing the determination of the float’s 20 position when it was at the surface (e.g. due to high sea-state) or the float’s failure to ascend and transmit data (e.g. due to sea-ice at high latitudes). Both situations lead to an unknown contamination of the displacement vector with drifts due to the near surface circulation.

All of the acoustically tracked floats recorded sound signal arrival times at least once per day. Thus, to generate a statistically consistent data set, we homogenized the underwater drift

time between all float types: For pop-up floats, we maintained their inherent drift period of 7 to 10 days; longer displacement periods were rejected due to the possible contaminations mentioned above. For acoustic floats we simulated the pop-up-float behaviour (Richardson, 1992) by subsampling the trajectories at a ten-day cycle, resulting in a sequence of float positions every 10  
5 days.

From the ensuing coherent data set of float positions, average velocities were calculated by dividing each underwater displacement vector by its corresponding duration (about 10 days, but the exact value was used for each displacement). Each velocity vector was assigned to the midway position between the start and end positions of the displacement vector. Velocities were  
10 quality checked by searching for velocities higher than  $2 \text{ m s}^{-1}$ ; no such value occurred.

As discussed above, pop-up float displacement vectors can be considered inherently independent due to drifts independent from the deep circulation during their ascent and surface phases. However, 10-day displacements from acoustically tracked floats can only be considered statistically independent, because the integral Lagrangian time scale has been shown to be equal  
15 or shorter than 10 days throughout the region and depth horizon considered here (Boebel et al, 1999c).

To extract the AAIW layer flow, float data was selected in the vertical according to three alternative schemes: two based on neutral density surfaces and another one based on isobaric surfaces (650 to 1050 dbars, following Boebel et al., 1999a). The hydrographic data base for  
20 these selections is described in the following section.

### ***Vertical data selection***

For the proper description and quantification of the AAIW's circulation, an appropriate definition of its vertical extent is of central importance. Salt and heat fluxes from the water layers above and below, as well as mixing with waters from the Indian Ocean render isohalines and

isotherms inappropriate as layer boundaries. Potential density surfaces, on the other hand, inadequately describe the vertical position of water masses without being referred to different pressure values. For example north of 5°S the surface of minimum salinity resides at a deeper depth than the isopycnal surfaces that best describes the AAIW layer at southern latitudes (Figure 1). Therefore, the AAIW core, when defined by its salinity minimum, not be tracked by a single potential density surface.

Neutral density surfaces have been shown to suitably describe the AAIW salinity minimum in the South Atlantic. For this reason, this paper uses gridded isoneutral surfaces of 1°×1° resolution at the core ( $\gamma^n = 27.40$ ), upper ( $\gamma^n = 27.25$ ) and lower boundaries ( $\gamma^n = 27.55$ ) of the AAIW layer, based on hydrographic fields from historic and contemporary data including the WOCE sections<sup>2</sup>. Two additional neutral density surfaces ( $\gamma^n = 27.32$  and  $\gamma^n = 27.45$ ) were calculated between the upper boundary and the core, as well as between the core and the lower boundary to provide further information on the vertical structure of the AAIW layer.

Based on these surfaces and on the average pressure during the displacement period, float displacement vectors were selected in the vertical (Figure 5, step 1). The primary data set was obtained by accepting only those float displacement vectors residing at depths within the AAIW layer as defined by upper and lower boundary neutral density surfaces, which maintained 68% of the original data. For comparison, additional data sets were obtained by either selecting according to isobaric surfaces or shifted isoneutral surfaces. For the latter, the upper and lower neutral surfaces were displaced by moving those surfaces 50 m up and down, respectively. This resulted in a 100 m thicker AAIW layer and an increased rate of accepted displacement vectors of 73%. The isobarically selected data set contained float displacements located between 650 and 1050 dbars (93% of the original data) as used in Boebel et al. (1999a). In the following we will

---

<sup>2</sup> You (2002) (3311 stations covering 70W-30E, 80S-0, see Figure 4) and correction for the surfaces around South Africa with data from You et al. (2003) (5684 stations covering 10W-50E, 50S-20S).

primary focus on the data set constrained by (unshifted) neutral density surfaces, and leave the comparison with the other data set to the final discussion.

### ***Geostrophic projection***

To test the influence of geostrophic shear within the AAIW layer on our results, the original 10-day displacement vectors were corrected using geostrophic velocity shear profiles, following the concepts employed by Gille (2002) and Richardson and Garzoli (2003) (see Figure 5, step 2). Firstly, geostrophic shear was calculated following You (2002) and You et al. (2003), i.e., using objectively mapped geostrophic velocity shear on neutral density surfaces ( $\gamma^n = 27.25, 27.32, 27.40, 27.45$  and  $27.55$ ) and fitting a cubic interpolation between the 5 geostrophic velocity values. Secondly, the geostrophic shear profile closest to the float's position was shifted (in velocity space) so that geostrophic shear and float velocity matched at float depth. The resulting (absolute) velocity of the shifted geostrophic profile at the AAIW's core (i.e., the salinity minimum core surface  $\gamma^n = 27.40$ ), is considered as the projection of the float velocity onto the AAIW core. The projected velocities differed only marginally from the original measures (on the order of  $0.01 \text{ cm s}^{-1}$  in almost the whole area (the Argentina Basin being the only exception, where the order is  $0.1 \text{ cm s}^{-1}$ )). These deviations yielded no detectable difference between space-time average maps, objective maps or transports (cf. discussion below) based on projected and unprojected data respectively. Hence, modifications due to the projection are ignored hereinafter.

20

## **Analysis**

### ***Space-time averaging***

The space-time averages were obtained by binning float velocity vectors according to their effective distance to the nodes of a regular grid (Figure 5, step 3). The effective distance between velocity vector and nodes was measured according to the norm developed by Davis (1998, his Formula 9)<sup>3</sup>:

$$5 \quad r^2 = |\vec{x}_a - \vec{x}_b|^2 + \left[ 3\mu \frac{H_a - H_b}{H_a + H_b} \right]^2 \quad ; \quad \mu \geq 0 \quad , \quad (1)$$

where  $\vec{x}_a$  is the position vector of the centre of a given cell,  $H_a$  the local smoothed water depth, and  $\vec{x}_b$  is the position vector of the centre of a given float displacement (where the water depth reads  $H_b$ ). This definition of the cells deforms the original rectangular boxes of the original grid to irregularly shaped cells (Figure 7) centred on the nodes of the regular grid. This approach follows the idea that currents tend to follow isobaths more likely than across them, as aptly exemplified in the extreme case of boundary currents.

The parameter  $\mu$  governs the sensitivity of the grid to the bathymetry: an increase in  $\mu$  causes a higher sensitivity of the grid to the bathymetry while  $\mu$  approaching zero causes a grid of higher regularity. The Smith and Sandwell (1997) bathymetry at 12 minutes resolution used herein has been smoothed to avoid the undesirable dependence on small scale bathymetric details. Following the study by Gille (2002), a 30 point Hanning filter was applied twice in latitudinal and longitudinal directions, effectively smoothing length scales of less than 1 degree in both directions.

Once binned, velocity vectors within each cell were averaged (Figure 5, step 4). The resulting space-time averaged velocity vector was positioned at the centre of gravity of the spatial

---

<sup>3</sup> What we show here is the formula as actually used by Davis (1998). The formula as displayed in Davis (1998) incorrectly features a variable 'L' from an alternative version (Davis, 2003, personal communication).

mean of all displacement vectors within each cell. Mean velocities based on less than 5 data points (i.e. less than 50 float-days worth of data), were discarded.

Space-time averages were calculated for a variety of different cell sizes of the initial regular grid, as well for various values of the parameter  $\mu$  (Table 2). Furthermore, the governing variable “bathymetry” was subsequently substituted by the potential vorticity of either the entire water column ( $f/H$ ) or of the AAIW layer ( $f/h$ ), building on LaCasce (2000) suggestion that the intermediate depth currents of the general circulation predominantly follow isolines of large-scale potential vorticity of the entire water column ( $f/H$ ).

The various choices of parametric values and variables resulted in a similar qualitative structure of the averaged currents field, though quantitative differences occurred. Hence a method to objectively determine the grid providing the “best” results is needed. To this end, LaCasce (2000) analysed mean displacements along and across isolines of potential vorticity and dispersions of stochastically modelled floats against time, and performed a statistical study of the tendency of those modelled floats to follow lines of equal potential vorticity. This concept is being followed here in a somewhat simplified fashion, by calculation of an alignment ratio  $A$ :

$$A = \frac{\overline{V_{\perp}}}{\overline{V_{\parallel}}} = \frac{\sum_{i=1}^n V_{\perp}^i}{\sum_{i=1}^n V_{\parallel}^i},$$

where  $V_{\perp}^i$  is the velocity component of the  $i$ th cell perpendicular to the isolines,  $V_{\parallel}^i$  is velocity component of the  $i$ th cell parallel to the isolines and  $n$  is the number of averaged velocities involved. This quantity is called *alignment number* hereinafter. It gives an idea of how well aligned the averaged velocity field is with respect to the isolines: the higher the alignment number, the less aligned the velocity field is, and the smaller the alignment number is, the better

aligned the velocity field is. The selection of an objectively “best” grid can then be reduced to finding the grid with the smallest alignment number (Figure 5, step 5).

We calculated  $f/h$  from the AAIW layer thickness of as defined by the distance between the upper and lower neutral density surfaces ( $\gamma^n = 27.25$  and  $\gamma^n = 27.55$ ). To calculate  $f/H$ , we used the smoothed bathymetry described above. In both cases, we took the Coriolis parameter as  $f = 2\Omega \sin(\lambda)$ , with  $\lambda$  being the latitude of the average velocity vector.

The selection of best grid, at an early stage of this study, was based on a subset of the data set described above. We assume that sufficient data was available at this time (65% of the actual data set) for an optimum selection of the grid. Results of this selection are shown in Table 2. The first two columns give the dimensions of the original rectangular cells before the deformation (for clarity, we have divided by boxes the results related to each original cell size). The third column indicates the value of  $\mu$  used to deform the cells. The next three columns specify the alignment number obtained under grids constructed with each of the variables (bathymetry,  $f/H$  and  $f/h$ ).<sup>4</sup> The minimum value for each variable and original grid size is marked in grey. Additionally, the overall minimum value for each original grid size is denoted in bold letters. As you can see, from 7 original grid sizes, the minimum alignment number was achieved 5 times for grids deformed under  $f/h$ , one time for grids deformed under  $f/H$  and one time for a grid deformed under bathymetry (though, actually without any deformation at all, since  $\mu = 0$ , i.e., it is a regular grid). This makes us believe that the best variable to use in Davis’ Formula is  $f/h$ , and that this physical variable has a bigger influence on the dynamics of the AAIW than  $f/H$  or bathymetry.

---

<sup>4</sup> The reason of why there are some blank cells in the table is the following: The degree of deformation of each of the grids varied different with  $\mu$ . This variation can not grow forever, since the deformation in grid boxes should not be so big that, for instance, you will get ringed boxes. Because of that, there was a point where we have stoped calculating grids for Bathimetry and  $f/H$ . Nevertheless,  $f/h$  is less sensible to variations in  $\mu$  and, hence, for this variable we had to calculate grids for higher values of  $\mu$  to get similar degrees of deformation as with the other two variables. Take into account, in any case, that what is important is to realize for which of the three variables we get the minimum allignement number.

Hence, for the space-time averages (Figure 5, step 6), we have chosen an initial regular grid of 3° in latitude and 4° in longitude, and we have deformed the cells under f/h with  $\mu = 6000$ . Finally, 0.63 probability error ellipses were calculated. Due to the statistical independence of all displacement vectors, the calculation of these ellipses was based directly on the number of displacement vectors per cell shown in Figure 6. Clearly, as seen in this Figure, the subtropical South Atlantic is covered well by the float data. To avoid redundant graphic representation and to improve readability, only the numbers of float days within each cell before deformation are given. The grid after deformation is depicted in Figure 7.

### ***Objective analysis and transport calculations***

The results of the space-time averages provided the data basis for objectively mapped velocity fields (Hiller and Käse, 1983) from which we derived objectively mapped stream functions. The graticule<sup>5</sup> was chosen by selecting 1 out of every 8 grid points of the softened bathymetry, yielding a graticule point every 1.7 ° in latitude (in a mean sense, since the Smith and Sandwell (1997) bathymetry is not regular in latitude) by 1.6° in longitude. The objective mapping (OM) correlation matrix was assumed Gaussian (Olbers et al., 1992), with the climatological error and correlation length of the climatological field defining the bell's amplitude and width, respectively. To optimise these parameters, we calculated almost 300 objective velocity maps, using subjectively chosen climatological value pairs (from 3 to 11 cm s<sup>-1</sup> for the climatologic error and 1° to 30° for the correlation length) (Figure 5, step 7). The error covariance we used is based on departures from the space-time averages in Figure 8. For each resulting velocity map, zonal and meridional volume transports were calculated.

For the transport calculation (Figure 11 to Figure 13, and step 8 in Figure 5), velocity was considered uniform across the AAIW layer. The thickness of the AAIW layer was calculated by

---

<sup>5</sup> For the objective mapping we use the word “graticule” and not “grid” to avoid confusions with the grid used to make the space-time average.

subtracting the depths of the deep boundary ( $\gamma^{\rho} = 27.55$ ) from that of the shallow boundary ( $\gamma^{\rho} = 27.25$ ). Velocities were multiplied by the thickness of each cell and the zonal and meridional widths of each cell, for meridional and zonal transport estimates respectively. Zonal and meridional transports along or across the basin were calculated by summarizing all transports (per cell) along a meridional or zonal section. In case of zonal, transoceanic sections, only those sections providing complete coverage along the chosen parallel were considered, i.e. the region from 25°S to 40°S (Figure 6). In longitude we have considered data just until 20°E (Cape Agulhas). Errors in the transports were calculated using Gauss' law of propagation of errors (Barlow, 1989) with the errors of the OA and the error of the thickness of the AAIW layer. The latter were assumed as 10 dbars, which is the general error of neutral density surfaces reported by Jacket and McDougall (1997).

The resulting transport estimates were compared against literature values (see section Transports below as well as Figure 9 and Figure 14). The analysis based on parameters providing the smallest squared error are used hereinafter (i.e. 4° correlation length and 3 cm s<sup>-1</sup> as climatological error) (Figure 5, step 9).

## Results

### *The large scale circulation*

Figure 8 shows averaged velocity vectors, as well as 0.63 probability error ellipses. Blue arrows represent flow with a westward zonal component, whereas red arrows indicate flow with an eastward zonal component. Isobaths of 1000 and 3000 meters are displayed. The Subtropical Gyre stands out clearly, with the eastward South Atlantic Current centred around 40°S and the westward Subtropical Gyre's northern branch just north of 30°S. In the South Atlantic Current the mean speeds are  $9.6 \pm 7.8$  cm s<sup>-1</sup>. The northern branch of the Subtropical Gyre is located between 22°S and 32°S and flows westward with a mean speed of  $4.7 \pm 3.3$  cm s<sup>-1</sup>. The Brazil

Current has a mean speed of  $11.6 \pm 7.4 \text{ cm s}^{-1}$  and flows, south of  $30^\circ\text{S}$ , parallel to the South American coast. The Benguela Current shows a speed of  $8.9 \pm 5.0 \text{ cm s}^{-1}$ , the Agulhas Current of  $25.3 \pm 14.2 \text{ cm s}^{-1}$  and the Agulhas Return Current of  $22.9 \pm 13.2 \text{ cm s}^{-1}$ . Currents in the tropical region are quasi zonal and of approximately  $3.5 \pm 2.2 \text{ cm s}^{-1}$  speed. These mean speeds and their root mean square errors (as well as those mentioned below) have been calculated through all the float raw velocities in the corresponding geographical region. The region has been chosen visually based on the velocity objective map (Figure 9), since the raw velocity field is too disordered to distinguish any tendency or current structure.

Figure 9 displays the results of the objective mapping, showing data only at those (objective map) graticule points positioned within a box (of the statistical grid, see Figure 6 and Figure 7) containing data. The objectively mapped velocity fields<sup>6</sup> depict the Subtropical Gyre comprising the region from  $23^\circ \pm 1^\circ\text{S}$  to  $46^\circ \pm 1^\circ\text{S}$  (the South Atlantic Current meanders from  $33^\circ\text{S}$  to  $46^\circ\text{S}$ ). The central part of the gyre (approximately along  $36^\circ\text{S}$ , see section “Transports” below) coincides with the AAIW layer’s region of greatest depth ( $\gamma^n = 27.40$ , i.e., the core, deeper than 900 dbars) and exhibits local recirculation cells (centred at  $35^\circ\text{S } 41^\circ\text{W}$ ,  $35^\circ\text{S } 29^\circ\text{W}$  and  $33^\circ\text{S } 10^\circ\text{W}$ ), that might provide short circuits for the Subtropical Gyre recirculation. The central ( $35^\circ\text{S } 29^\circ\text{W}$ ) recirculation pattern is also present in the geostrophic velocity field that Defant (1941) calculated. Just north of the Subtropical Gyre an eastward current located near  $20^\circ\text{S}$  (between  $10^\circ\text{W}$  and  $0^\circ\text{W}$ ) is present, with a speed of  $4.0 \pm 2.4 \text{ cm s}^{-1}$  (c.f. Richardson and Garzoli (2003)). Most notably is the intensification of the Subtropical Gyre along the western boundary, while the eastern closure appears to spread out over several branches.

---

<sup>6</sup> Mean speeds are underestimated in the objective maps. This is a characteristic of the method (especially when applied to an extended area such as the entire Subtropical South Atlantic). Therefore, as mentioned above, mean speeds are discussed within the framework of float raw data, rather than that of objective maps.

These differences stand out even more clearly in the stream function. This is shown in Figure 10, where we represented negative contourlines of the stream function embracing the Subtropical Gyre in blue and positive contourlines in red. Streamlines are closed and squeezed in the Brazil Current Region, while the stream function features a broad col in the Cape Basin, with no contourline connecting the Agulhas Current to the nascent Benguela Current. This observation supports the notion of the Cape Basin as a region of turbulent inter-ocean exchange (i.e. the Cape Cauldron, Boebel et al., 2003) where eddy fluxes dominate both the closure of the Subtropical Gyre as well as the spicing up of fresh Atlantic AAIW with salty Indian Ocean AAIW (Lutjeharms, 1996). Contrastingly, the innermost streamlines of the Subtropical Gyre close in the western part of the Cape Basin, near the Walvis Ridge, and hence provide a direct advective route for AAIW to recirculate.

A possible Tropical Gyre is hinted by quasi-closed streamlines farther north (reaching diagonally across the Atlantic). The gyre seems to be divided into a western and eastern subcell. While sparse data at these latitudes on the eastern side of the basin do not permit reliable conclusions, the observations do not contradict the concept of three subcells as proposed by Suga and Talley (1995).

### ***Transports***

To match the objectively mapped velocity field, the stream function (Figure 10) was calculated using the velocities and not the barotropic transports. Hence, if you want to estimate transports from the stream function, you have to multiply the difference in value of two isolines by the AAIW layer thickness (approximately 0.5 Km). Nevertheless, as explained in the Analysis Section, we have estimated transports directly from the velocity field in a more accurate fashion,

using a layer with non constant thickness defined by the isoneutral surfaces. The results obtained like this are discussed next.

Figure 11 depicts the mean zonal transport per degree latitude (for clarity, error bars are not shown). For the southern branch of the Subtropical Gyre (i.e., the South Atlantic Current) the area under the curve is approximately  $13 \text{ Sv} \pm 3 \text{ Sv}$  (east), whereas for the northern branch is  $12 \text{ Sv} \pm 2 \text{ Sv}$ . Errors were calculated through the square root of the sum of all the objectively mapped errors. These values suggest a surprisingly well balanced northern and southern branches of the Subtropical Gyre.

The core of the South Atlantic Current, as identified by the maximum mean zonal transport, is located at  $44^\circ\text{S}$ . Analogously, at around  $29^\circ\text{S}$ , the mean zonal transport is a minimum, unveiling the core of the northern branch of the Subtropical Gyre. These values are in good agreement with the observations from Boebel et al. (1999a). As already discussed with our results from the OA, the Subtropical Gyre seems to be centred at about  $36^\circ\text{S}$ , the latitude where the mean zonal transport changes sign. This is in contrast with the  $30^\circ\text{S}$  from Reid, 1996 and Boebel, 1997 and in good agreement with results from Reid, 1989 ( $34^\circ\text{S}$ ), Schmid, 1998 and Schmid et al, 2000 ( $35^\circ\text{S}$ ) as well as Boebel et al., 1999c ( $35^\circ\text{S}$ ). Nevertheless, it is worth noting the inappropriateness of defining a singular latitude for the centre of the Subtropical Gyre. As visible in Figure 9 and Figure 14 this axis is actually slightly sloped in latitude (as also noticed by Boebel, et al, 1999c).

The meridional transport is depicted in Figure 12 with positive transports pointing northwards. The general structure of the meridional transport is governed by a large scale trend of southward transports south of  $28^\circ\text{S}$ , and northward transports north of this latitude. Superposed to this tendency are smaller scale variations (order of  $5^\circ$  length scale).

The local minimum at about 35°S (i.e. the mean axes of the Subtropical Gyre (See Figure 9)) most probably reflects the dominance of the intensive South Brazil Current. North of this latitude up to 30°S, the transport grows with positive values dominating.

5

## Discussion

The resulting general structure of a basin wide Subtropical Gyre with an adjacent quiescent flow regime to the north (the tropical region) falls in line with concepts developed in many previous hydrographic and tracer (Rose, 1999; Schlosser et al., 2000) studies, but here, for the first time, analysis of Lagrangian velocities reveals the flow structure of the entire Subtropical Gyre at mid depth.

A direct comparison of our transport estimates with calculations from the literature is obscured by the diversity of measurement and analysis methods used: Lagrangian and Eulerian measurements, inverse models and geostrophy. Additionally, the definition of the AAIW layer (i.e. vertical boundaries) varies as well. For these reasons, a general agreement of the transports calculated here with those found in the literature would be surprising. Figure 13 compares ours with literature values, displaying error bars when available and a shaded error area for our estimates. The literature results are based on model and inverse model calculations. In a general sense, our meridional transports are always smaller than those found in the literature. Even though this could be related to the different AAIW layer definitions, we believe that the two most likely reasons for this discrepancy are: a) the sub-estimation of velocity estimates by the OA and b) the poor resolution of the chosen best grid, causing an under-evaluation of the influence of the intermediate western boundary current (IWBC). This western boundary current is thought to transport the major bulk of AAIW across the equator (Defant, 1941, Gordon and Bosley, 1991, Boebel, et al., 1999c, Jochum et al., 2003 ).

In an attempt to compensate this underestimation of the AAIW flow within the IWBC, for latitudes northern than 28°S we added the assumed transport of 4 Sv (Boebel et al., 1999a) to our curve north of 28°S (Figure 13). This yields in a positive transport for the whole region north of the Santos Bifurcation and in a fair agreement with results from Macdonald, 1993, Vanicek and Siedler, 2002 and Roemlich, 1983.

Comparing the meridional transport results of float data selected according to neutral density surfaces with those from data selected by isobaric surfaces (Figure 12), shows virtually identical results between 17°S and 40°S. On the other hand, the transport calculations obtained via neutral density based selection but surfaces expanded 50 meters up and down (not shown) differ significantly in relation with the other two data sets throughout the entire domain. Judging this later data set to comprise significant amounts of adjacent water masses, we discarded this data set altogether.

Figure 14 shows the results of the objective mapping for the data set as constrained by pressure surfaces. The main differences among these results and those obtained under the neutral density constraints (Figure 9) are a) a weaker eastward current just north of the Subtropical Gyre (near 20°S and east of the Mid-Atlantic Ridge), b) currents north of 10°S show more structure and are mainly zonal, c) the anticyclonic Zapiola Eddy is observed around 45°S and 45°W, and d) part of the Falkland/Malvinas current emerge between 40 and 45°S.

These results obviously reflect themselves in the transport estimates (Figure 12): south of 40°S the maximum negative value in the meridional transport calculated with the neutral density set is around -12 Sv at 43°S, whereas that happens at 45°S in the case of the transport calculated with the pressure set (with a higher value of -20 Sv). This is also patent in the mean zonal transport (Figure 11): at around 44°S the mean zonal transport is a maximum for the neutral density set and points eastwards, whereas under the pressure selection the transport reaches its

maximum even southern (47°S). As with the extended neutral density set (but to a smaller degree), we believe that all these discrepancies in currents and their corresponding transports are due to the contamination in the pressure-selected set with currents that belong to other water masses. For instance, at southern latitudes the AAIW tends to surface and selecting the float data  
5 by pressure at this area yields currents from layers beneath the AAIW. As defined by neutral density surface, AAIW lies above 400 m southern from 45°S and since the floats are drifting always at more than 500 m, we do not have any float data inside the AAIW at this zone. In the case of the pressure selection, on the contrary, we had many float data in the same zone. This is the reason of why the Falkland/Malvinas Current is partially visible only on the objective map  
10 constrained by isobaric (Figure 14) surfaces and not in the on constrained by neutral density surfaces (Figure 9).

### Summary

A float data set of 451 float years, collected over a period of two decades and finally covering  
15 the entire subtropical South Atlantic, has been gathered. The data set comprises results from historical as well as recent pop-up and acoustically tracked floats. We confined these data by three different vertical selection criterions: isobaric surfaces (650 to 1050 dbars), neutral density surfaces ( $\gamma^n = 27.40$  to  $\gamma^n = 27.55$ ) and neutral density surfaces with an expanded layer thickness (50 m up and 50 down from the aforementioned neutral density surfaces, respectively).

20 Space-time averages were performed within grid cells of different size and shapes, following isolines of bathymetry,  $f/H$  and  $f/h$  in a different degree. The quality of the grid was assessed through calculation of the alignment of the mean velocities relative to the cell shaping field. We concluded that the grids yielding the best results are those following  $f/h$ . Within this

group, a grid of  $3^\circ$  latitude  $\times$   $4^\circ$  longitude outperformed the others, and was therefore selected to compute space-time averages, error ellipses, as well as meridional and zonal transports.

Subsequently, we objectively mapped these space-time averages using multiple sets of parameters. We have calculated approximately 300 objective maps. For each of them, using the  
5 thickness of the AAIW as defined by the neutral density surfaces, we calculated zonal and meridional transports. Rms differences between meridional transport estimates and estimates from literature were calculated. Minimum rms differences were yielded when a correlation length of  $4^\circ$  and a climatological variability of  $3 \text{ cm s}^{-1}$  were assumed.

These analyses reveal a Subtropical Gyre of  $12 \text{ Sv} \pm 2 \text{ Sv}$  (mean speed of  $4.7 \pm 3.3 \text{ cm s}^{-1}$ )  
10 in the northern branch and  $13 \text{ Sv} \pm 3 \text{ Sv}$  ( $9.6 \pm 7.8 \text{ cm s}^{-1}$ ) in the South Atlantic Current, within the AAIW layer (confined by the  $\gamma^\sigma = 27.25$  and  $\gamma^\sigma = 27.55$  isoneutral surfaces). The Gyre seems to be centred in a mean latitudinal sense near  $36^\circ\text{S}$ , spanning from  $23^\circ \pm 1^\circ\text{S}$  to  $46^\circ \pm 1^\circ\text{S}$ . Evidence of the existence of a Tropical Gyre divided in two subcells by the Midatlantic Ridge is visible on the stream function, where the western intensification stands out clearly.

15 When compared with transports found in the literature across transoceanic sections, as a rule our results are always smaller. The reasons might be related to the way in which the different authors have bounded the AAIW, but most probably to the fact that the objectively mapped velocities are in general an underestimation of the measured velocities and the fact that our space-time average was unable to unveil the IWBC.

20 The main differences among the results obtained under the two data sets (pressure and neutral density) are the absence of the Malvinas Current and the Zapiola Eddy on the results obtained with neutral density set. We attribute this to the vertical structure of the AAIW layer at southern latitudes. The pressure selection of float data in the vertical seems to be a good choice for the AAIW in the South Atlantic just for the area between  $17^\circ\text{S}$  and  $40^\circ\text{S}$ , since the results

obtained with this data set are very similar to those obtained with the data set selected under neutral density surfaces. Southern and northern from this area results are very different between the two data sets.

### **Acknowledges**

5 We would like to express our gratitude to all the crews, officers, research assistants and researchers contributing to the collection and archiving of float data. In particular, we would like to thank Claudia Schmid for giving us the first data set from AOML/Argo, with which this work started in 2002, as well as Igor Belkin and Reiner Schlitzer (the latter, for his extensive advice related to objective mapping). This work is supported through NSF-Grant no. OCE-0095647 and  
10 through the Alfred Wegener Institute for Polar and Marine Research. One of us (Olaf Boebel) would like to thank Walter Zenk for providing the opportunity to start a career in oceanography and for many years of thoughtful mentoring.

### **Appendix**

15 Antarctic Intermediate Water was first identified in the South Atlantic and its discovery is usually assigned to either Wüst or Deacon, based on data collected during the 1925-1927 RV Meteor and Discovery expeditions. However, such assignments provide only an incomplete view. While both, Deacon and Wüst (probably independently) developed the first enduring theory on the AAIW's origins, they did not identify the water mass for the first time. In fact, the vertical  
20 salinity minimum was first measured during the 1872-1876 Challenger expedition (Buchanan, 1877; according to Talley, 1996). Later measurements during the second German expedition to Antarctica (1911-1912), directed by Wilhelm Filchner onboard the "Deutschland", detected the salinity minimum as well. Analysing these data, Brennecke (1921) describes the motion at the salinity minimum layer as a "sub-Antarctic deep current" and "gives its origin as the surface drift

out of the Weddell Sea” (cited from Deacon, 1933, page 222). Only thereafter, Merz and Wüst (1922) published a complete meridional section of salinity, from which it was possible to identify the extent of the salinity minimum (Talley, 1996). Later, Erich von Drygalski based on data from the first German expedition to Antarctica (1901-1903) aboard “Gauss”, describes (the water mass related to the salinity minimum as being of Antarctic origins (von Drygalski, 1927, according to Deacon, 1933). Hence, when discussing the discovery of AAIW it would be fair to attribute it either to Buchanan (1877) or Brennecke (1921) (as he probably was the first researcher to provide a theory about AAIW’s origins).

10

### References

Barlow, R. J., 1989. Statistics. A guide to the Use of Statistical Methods in the Physical Sciences, John Wiley and Sons.

15 Barnier, B., P. Marchesiello and A. Pimenta de Miranda. (1996). "The Impact of Seasonal Forcing on the Variability of the Meridional Heat Flux at 30°S Using a Sigma-Coordinate Primitive Equation Model." International WOCE Newsletter(24): 16-23.

20 Boebel, O., C. Schmid and W. Zenk, 1997. Flow and recirculation of Antarctic Intermediate Water across the Rio Grande Rise. Journal of Geophysical Research, Vol. 102, No. C9, pages 20,967 - 20,986.

Boebel O., R. E. Davis, M. Ollitrault, R. G. Peterson, P. L. Richardson, C. Schmid and W. Zenk, 1999a. The Intermediate Depth Circulation of the Western South Atlantic. Geophysical Research Letters, Vol. 26, No. 21, pages 3329-3332.

Boebel, O., C. Schmid, G. Podestá and W. Zenk, 1999b. Intermediate water in the Brazil-Malvinas Confluence Zone: A Lagrangian view. *Journal of Geophysical Research*, Vol. 104, No. C9, Pages 21,063-21,082.

5

Boebel, O, C. Schmid and W. Zenk, 1999c. Kinematic elements of Antarctic Intermediate Water in the western South Atlantic. *Deep-Sea Research II*, 46, pages 355-392.

Boebel O., J. Lutjeharms, C. Schmid, W. Zenk, T. Rossby and C. Barron, 2003. The Cape  
10 Cauldron: A regime of turbulent interocean exchange. *Deep-Sea Research II* 50(1): 35-56.

Buchanan, J.Y., 1877. On the distribution of salt in the ocean, as indicated by the specific gravity of its waters. *J. Roy. Geogr. Soc.* 47: 72:86.

15 Brennecke, W.,1921. Die ozeanographischen Arbeiten der Deutschen Antarktischen Expedition 1911-1912. Aus dem Archiv des Deutschen Seewarte, 39, 216pp. Hamburg.

Davis, R. E., D. C. Webb, L.A. Regier and J. Dufour, 1992. The Autonomous Lagrangian Circulation Explorer. *Journal of Atmospheric and Oceanic Technology* 9: 264 - 285.

20

Davis, R. E., Killworth, P. D., Blundell, J. R., 1996. Comparison of Autonomous Lagrangian Circulation Explorer and Fine Resolution Antarctic Model results in the South Atlantic. *Journal of Geophysical Research* 101(C1): 855 - 884.

Davis, R. E., 1998. Preliminary results from directly measuring mid-depth circulation in the tropical and south Pacific. *Journal of Geophysical Research* 103(C11): 24619-24639.

5 Deacon, G. R. E., 1933. A general account of the hydrology of the South Atlantic Ocean, *Discovery Rep.*, 7, 171-238.

Defant, A., 1941. Quantitative Untersuchungen zur Statik und Dynamik des Atlantischen Ozeans, in *Wiss. Ergebn. Dtsch. Atlant. Exped. „Meteor“*, vol 6, pp. 191-260, Walter de Gruyter, Berlin, Germany.

10

Fu, L., 1981. The general circulation and meridional heat transport of the subtropical South Atlantic determined by inverse methods. *Journal of Physical Oceanography* 11: 1171-1193.

15 Gille, S. T., 2002. Float Observations of the Southern Ocean, Part1: Estimating Mean Fields, Bottom Velocities and Topographic Steering. *Journal of Physical Oceanography* (In press).

Gordon, A. L. and K. T. Bosley, 1991. Cyclonic gyre in the tropical South Atlantic. *Deep Sea Research* 38: 323-343.

20 Gould, John. *Deep Sea Research II*. This volume.

Hiller, W. and R. H. Käse, 1983. "Objective Analysis of Hydrographic Data Sets from Mesoscale Surveys." *Berichte aus dem Institut für Meereskunde an der Christian-Albrechts-Universität Kiel* 116: 78 pp.

25

- Holfort, J., 1994. Großräumige Zirkulation und meridionale Transporte im Südatlantik., Abt. Meeresphysik. Kiel, Institut für Meereskunde: 96.
- Jackett, D. R. and T. J. McDougall, 1997. A neutral density variable for the world's oceans. 5 Journal of Physical Oceanography 27(2): 237-263.
- Jochum, M. and P. Malanotte-Rizzoli, 2003. The flow of AAIW along the equator. Interhemispheric Water Exchanges in the Atlantic Ocean. Elsevier Series.
- 10 LaCasce, 2000. Floats and f/H. Journal of Marine Research 58: 61-95.
- Lutjeharms, J.R.E., 1996. The Exchange of Water Between the South Indian and South Atlantic Oceans. The South Atlantic: present and past circulation. G. Wefer, W. H. Berger, G. Siedler and D. Webb. Berlin-Heidelberg, Springer-Verlag: 219-238.
- 15 Macdonald, A. M., 1993. Property fluxes at 30°S and their implications for the Pacific-Indian troughflow and the global heat budget. Journal of Geophysical Research 98: 6851-6868
- Matano, R. and G. Philander, 1993. Heat and mass balances of the south Atlantic ocean 20 calculated from a numerical model. Journal of Geophysical Research 98(C1): 977-984.
- McDougall, T. J., 1987. Neutral surfaces. Journal of Physical Oceanography 17(11): 1950-1964.

- Merz, A. and G. Wüst., 1922. Die atlantische Vertikalzirkulation. Zeitschr. Ges. f. Erdkunde: pp. 1-35
- Molinari, R. L., B. Voituriez, and P. Duncan, 1981. Observations in the subthermocline undercurrent of the equatorial South Atlantic Ocean: 1978-1980. *Oceanologica Acta* 4: 451-456.
- Olbers, D., V. Gouretski, G. Seiß, J. Schröter, 1992. Hydrographic Atlas of the Southern Ocean. Bremerhaven, Alfred Wegener Institut.
- Ollitrault, M., 1994a. The Topogolf Experiment: Lagrangian Data. Brest, France, IFREMER - Centre de Brest.
- Ollitrault, M., G. Loaëc and C. Dumortier, 1994b: MARVOR: a multi-cycle RAFOS float. *Sea Technology*, 35(2), 39-40, 43-44.
- Ollitrault, M., 1995. The Samba Experiment. Volume 1: Samba 1 Lagrangian and CTD data (February 1994-August 1995). IFREMER. Brest.
- Ollitrault, M., 1999. MARVOR floats reveal intermediate circulation in the western equatorial and tropical south Atlantic (30S to 5N). *WOCE Newsletter* 34, 7-10.
- Reid, J. L., 1989. On the total geostrophic circulation of the South Atlantic Ocean: Flow patterns, tracers, and transports, *Prog. Oceanogr.*, 23 (3), 149-244.

Reid, J. L., 1994. On the total geostrophic circulation of the North Atlantic Ocean: Flow patterns, tracers and transports. *Progress in Oceanography* 33: 1 - 92.

5 Reid, J. R., 1996. On the circulation of the South Atlantic Ocean. *The South Atlantic: Present and past circulation*. G. Wefer, W. H. Berger, G. Siedler and D. J. Webb. Berlin Heidelberg, Springer-Verlag: 13 - 44.

10 Richardson, P. L., 1992. Velocity and eddy energy of the Gulf Stream System from 700-m SOFAR floats subsampled to simulate Pop-Up floats. *Journal of Atmospheric and Oceanic Technology* 9: 495-503.

Richardson, P. L. and W. J. Schmitz, 1993. Deep cross-equatorial flow in the Atlantic measured with SOFAR floats. *Journal of Geophysical Research* 98: 8371 - 8388.

15 Richardson, P. L. and S. L. Garzoli, 2003. Characteristics of Intermediate Water flow in the Benguela Current as measured with RAFOS floats. *Deep Sea Research II* 50(1): 87-118.

Rintoul, S. R., 1991. South Atlantic interbasin exchange. *Journal of Geophysical Research* 96: 2675-2692.

20 Roemmich, D., 1983. The balance of geostrophic and Ekman transports in the tropical Atlantic ocean. *Journal of Physical Oceanography* 13: 1534-1539.

Rose, H., 1999. Untersuchung der Zirkulation und der Erneuerung des Antarktischen Zwischenwassers im Südatlantik aus FCKW-Daten. PhD. Thesis. Universität Bremen, Fachbereich 1. Institut für Umweltphysik.

- 5 Rossby, T. and D. C. Webb, 1970. Observing Abyssal Motions by Tracking Swallow Floats in the SOFAR Channel. *Deep-Sea Research* 17: 359-365.

Rosby, H. T., E. R. Levine, et al., 1985. "The isopycnal Swallow Float - a simple device for tracking water parcels in the ocean." *Progress in Oceanography* 14: 511-525.

10

Rosby, H.T., Dorson, D. and Fontaine, J., 1986. The RAFOS System. *Journal of Atmospheric and Oceanic Technology* 3(4): 672-679.

- Schlitzer, R., 1996. Mass and Heat Transports in the South Atlantic Derived from Historical Hydrographic Data. *The South Atlantic. Present and Past Circulation*. G. Wefer, W. H. Berger, G. Siedler and D. J. Webb, Springer.

- Schlosser, P., J. L. Bullister, R. Fine, W.J. Jenkins, R. Key, J. Lupton, W. Roether, W.M. Smethie, 2000. Transformation and Age of Water Masses. *Ocean Circulation and Climate*. G. Siedler, J. Church and J. Gould, Academic Press.

20

Schmid, C., 1998. Die Zirkulation des Antarktischen Zwischenwassers im Südatlantik. Dept. of Ocean Physics. Kiel, University of Kiel: 104.

- Schmid, C., G. Siedler and W. Zenk, 2000. Dynamics of intermediate water circulation in the subtropical south Atlantic. *Journal of Physical Oceanography*. Vol. 30, No. 12. pp. 3191-3211.
- Schmid, C., R. L. Molinari and S. L. Garzoli, 2001. New observation of the intermediate depth  
5 circulation in the tropical Atlantic. *Journal of Marine Research*, 59, pp 281-312.
- Smith, W. H. F. and D. T. Sandwell, 1997. Global seafloor topography from satellite altimetry and ship depth soundings, *Science*, v. 277, p. 1957-1962, 26 Sept., 1997.
- 10 Stramma, L. and R. G. Peterson, 1989. Geostrophic transport in the Benguela Current Region. *Journal of Physical Oceanography* 19: 1440-1448.
- Stramma, L., and R. Peterson, 1990. The South Atlantic Current, *J. Phys. Oceanogr.*, 20, 846-859.
- 15 Suga, T. and L. D. Talley, 1995. Antarctic Intermediate Water circulation in the tropical and subtropical South Atlantic. *Journal of Geophysical Research* 100(C7): 13441-13453.
- Talley, L. D., 1996. Antarctic Intermediate Water in the South Atlantic. *The South Atlantic: present and past circulation*. G. Wefer, W. H. Berger, G. Siedler and D. Webb. Berlin-Heidelberg, Springer-Verlag: 219-238.
- 20 Tomczak, M. and J.S. Godfrey, 1994. *Regional Oceanography: An introduction*. Pergamon. First Edition.

Vanicek, M. and G. Siedler, 2002. Zonal fluxes in the deep water layers of the western south atlantic ocean. *Journal of Physical Oceanography* 32: 2205-2235.

5 Von Drygalski, E. V., 1927. *Deutsche Südpolar Expedition, 1901-1903, VII, Ozeanographie.*

Wüst, G., 1935. <sup>7</sup> Schichtung und Zirkulation des Atlantischen Ozeans, Die Stratosphäre, in *Wissenschaftliche Ergebnisse der Deutschen Atlantischen Expedition auf dem Forschungs- und Vermessungsschiff „Meteor“ 1925-1927, vol. 6, pp. 109-288, Walter de Gruyter, Berlin, 1935.*

10

You, Y., 1998. Intermediate water circulation and ventilation of the Indian Ocean derived from water-mass contributions. *Journal of Marine Research* 56, 1029-1067.

15 You, Y., 2002. "Quantitative estimate of Antarctic Intermediate Water contributions from the Drake Passage and the southwest Indian Ocean to the South Atlantic." *Journal of Geophysical Research* 107(C4).

20 You, Y., J. Lutjeharms, O. Boebel, W. P. M. de Ruijter, 2003. Quantification of the interocean exchange of intermediate water masses around southern Africa. *Deep-Sea Research II* 50(1): 197-228.

Zhang, D., M. J. McPhaden, W. E. Johns, 2002. Interior Ocean Pycnocline Transports in the Atlantic Subtropical Cells. *Clivar Exchanges. Selected Research Papers.*

---

<sup>7</sup> English translation edited by William J. Emery: "The stratosphere of the Atlantic Ocean. Scientific Results of the German Atlantic Expedition of the Research Vessel 'Meteor' 1925-27". Published by Amerind Publishing Co., 1978.

Zenk, W., Schmid, C., Boebel, O., 1998. WOCE floats in the South Atlantic. International WOCE Newsletter 30, 39–42.

## Figures

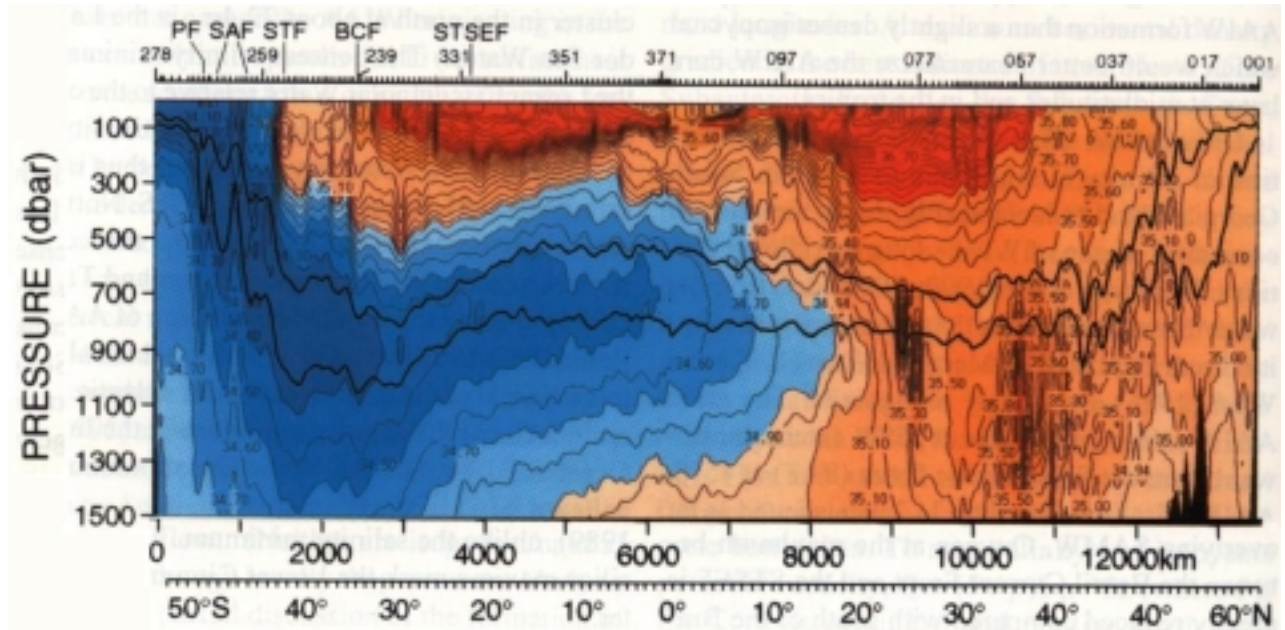


**Figure 1. Meridional section of salinity along approximately 25°W, from South Georgia Island to Iceland, from 1988-1989. The two curves passing through the AAIW are the 31.7 and 31.9  $\sigma_1$  isopycnal contours. Modified from Talley (1996, her Figure 1 (a)).**

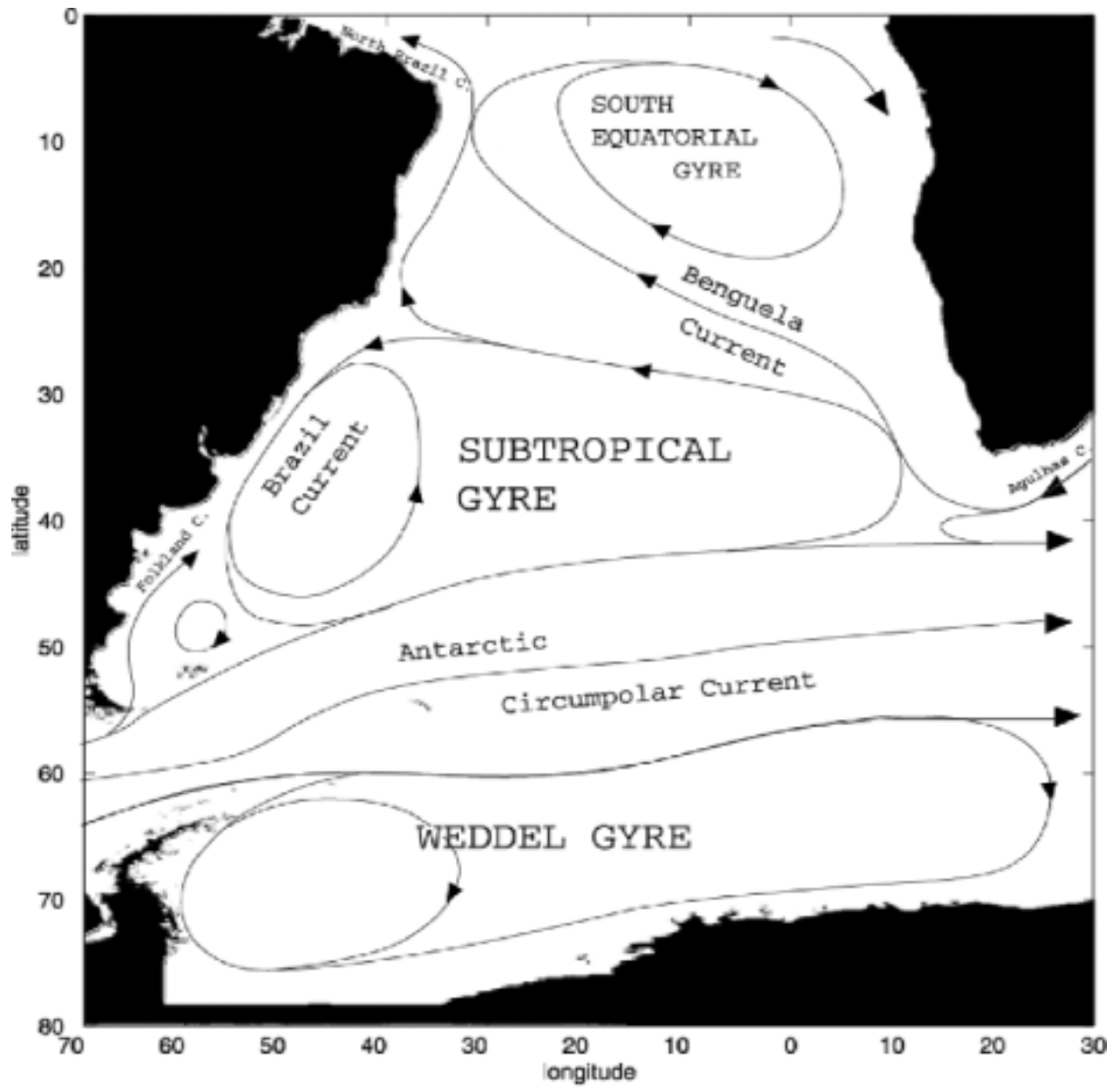


Figure 2. Schematics of AAIW circulation in the South Atlantic (adapted from You (2002)).

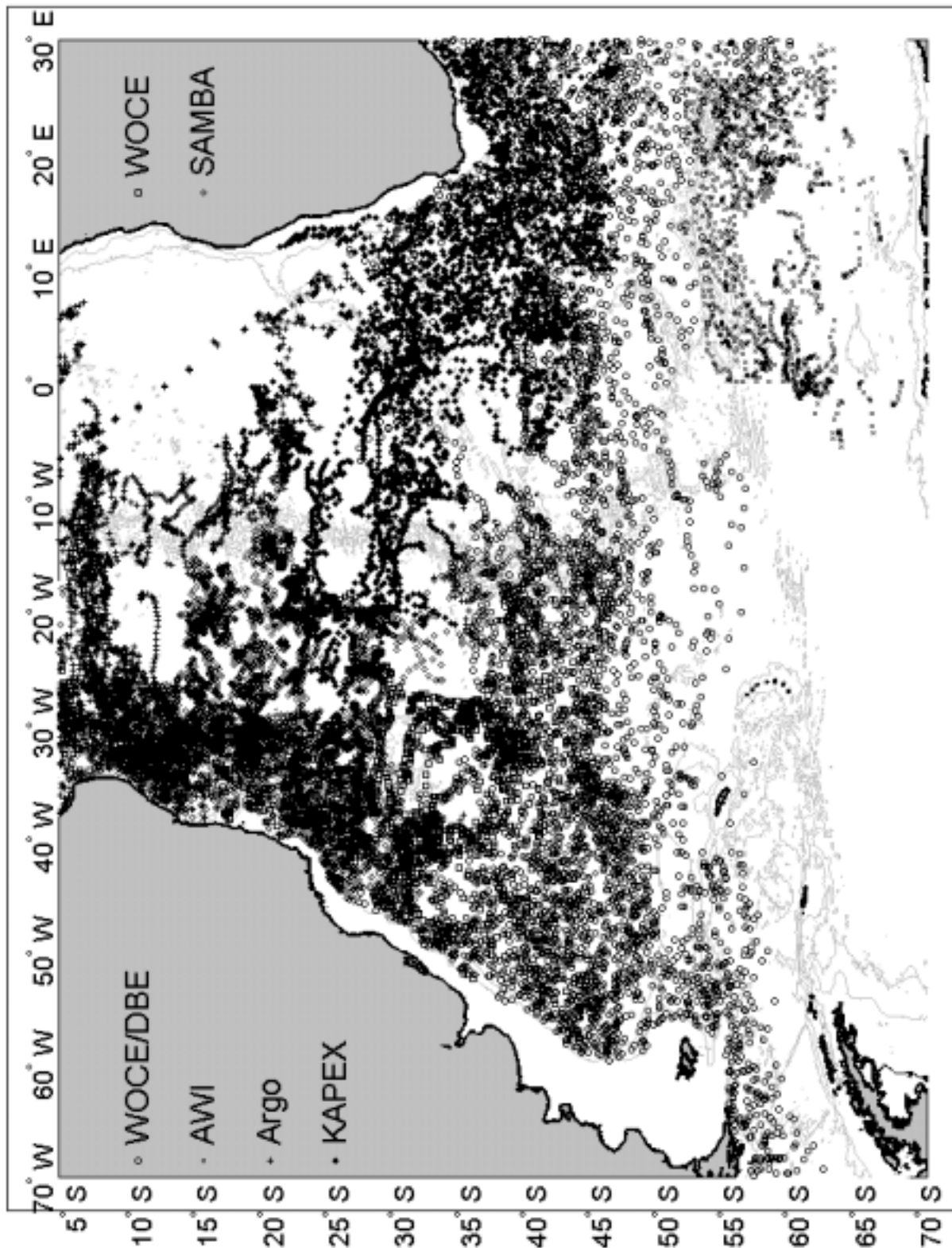


Figure 3. Float trajectory data without vertical selection. Most of the floats drifted between 400 and 1200 dbars with displacement periods of 10 days. For clarity, only descent positions are shown. Each of the six float programs is symbolized by a unique identifier, but high data density renders individual trajectories indistinguishable.

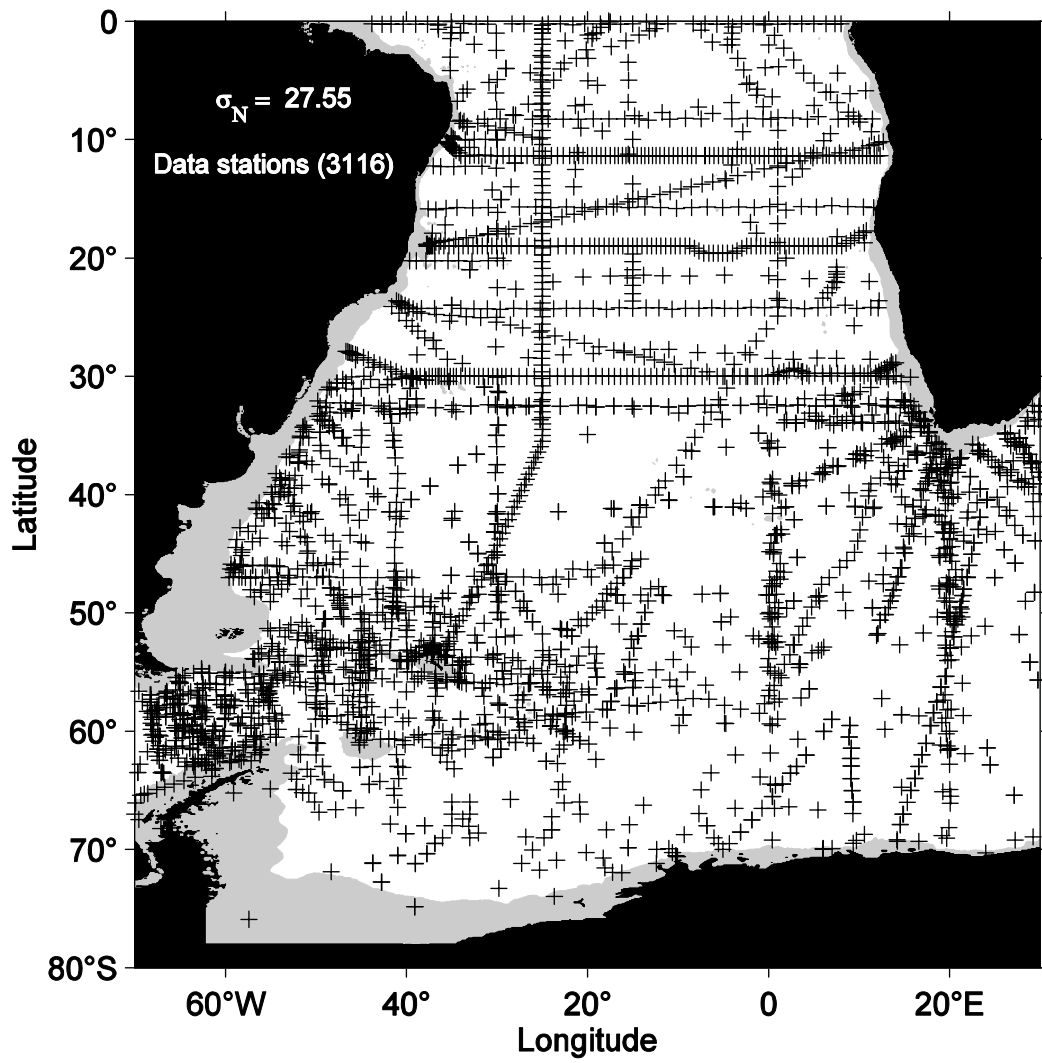
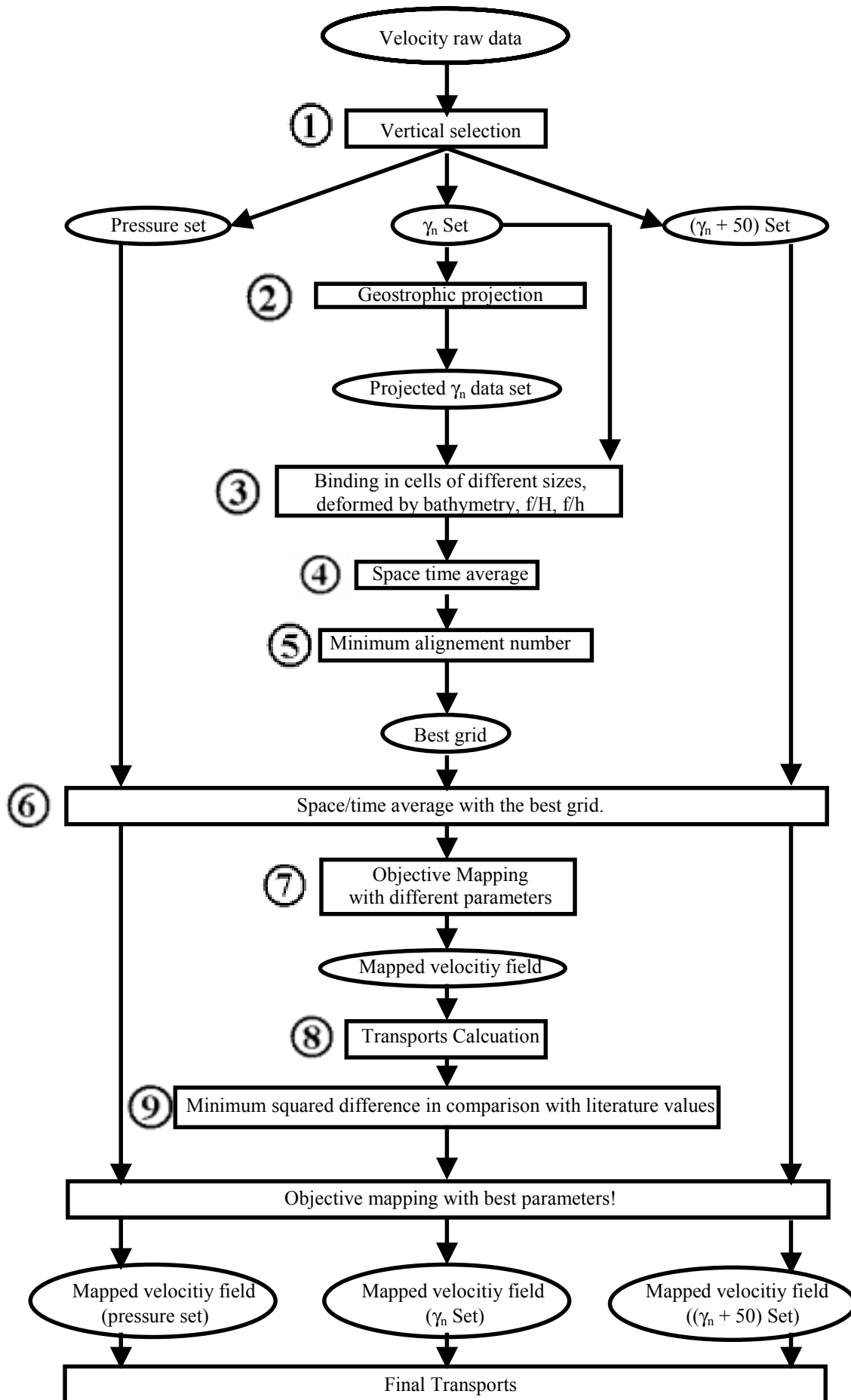


Figure 4. Hydrographic stations used in You, 2002, (his figure 2) to extract neutral density surfaces for AAIW.



**Figure 5** Flow chart of float data processing. Data sets are denoted with ellipses and data processes with rectangles. As a reference in the text, for each process step there is a number in a circle.



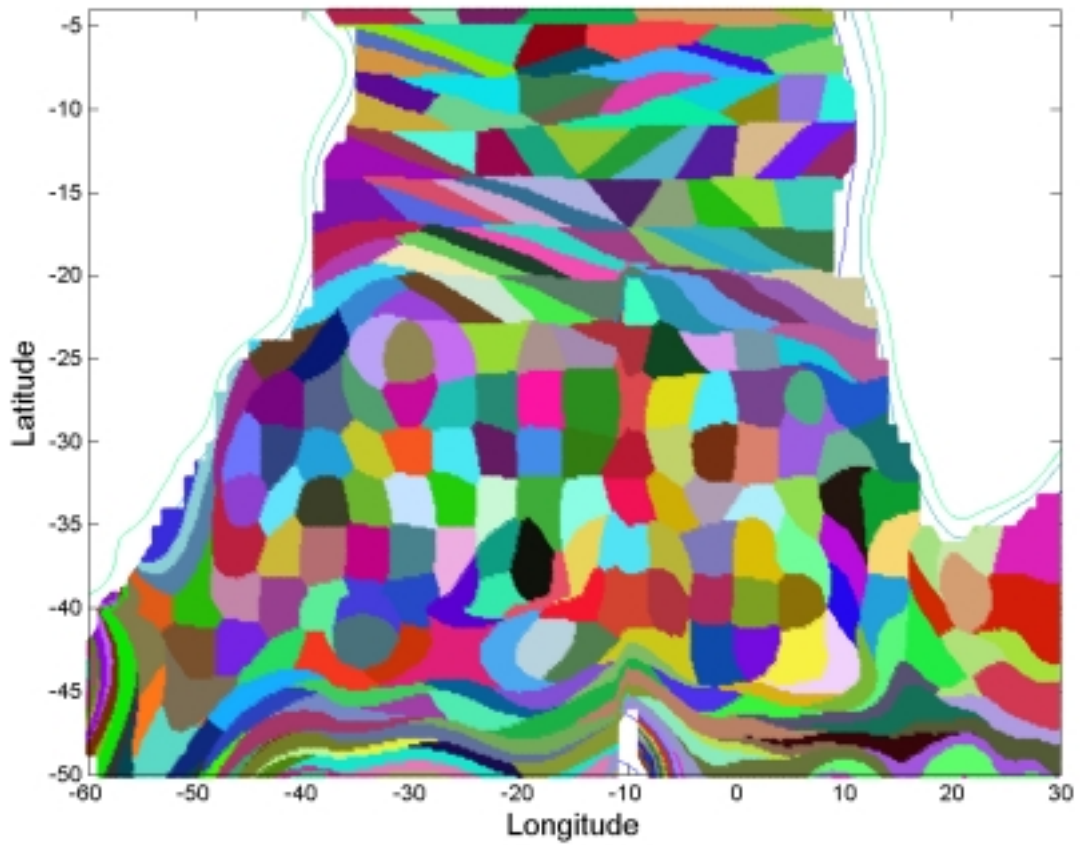


Figure 7. Grid used for space-time average of the final results. Cells are based on an initial regular grid of  $3^\circ$  (latitude)  $\times$   $4^\circ$  (longitude) and deformed using Formula 1 with  $f/h$  and  $\mu = 6000$ .

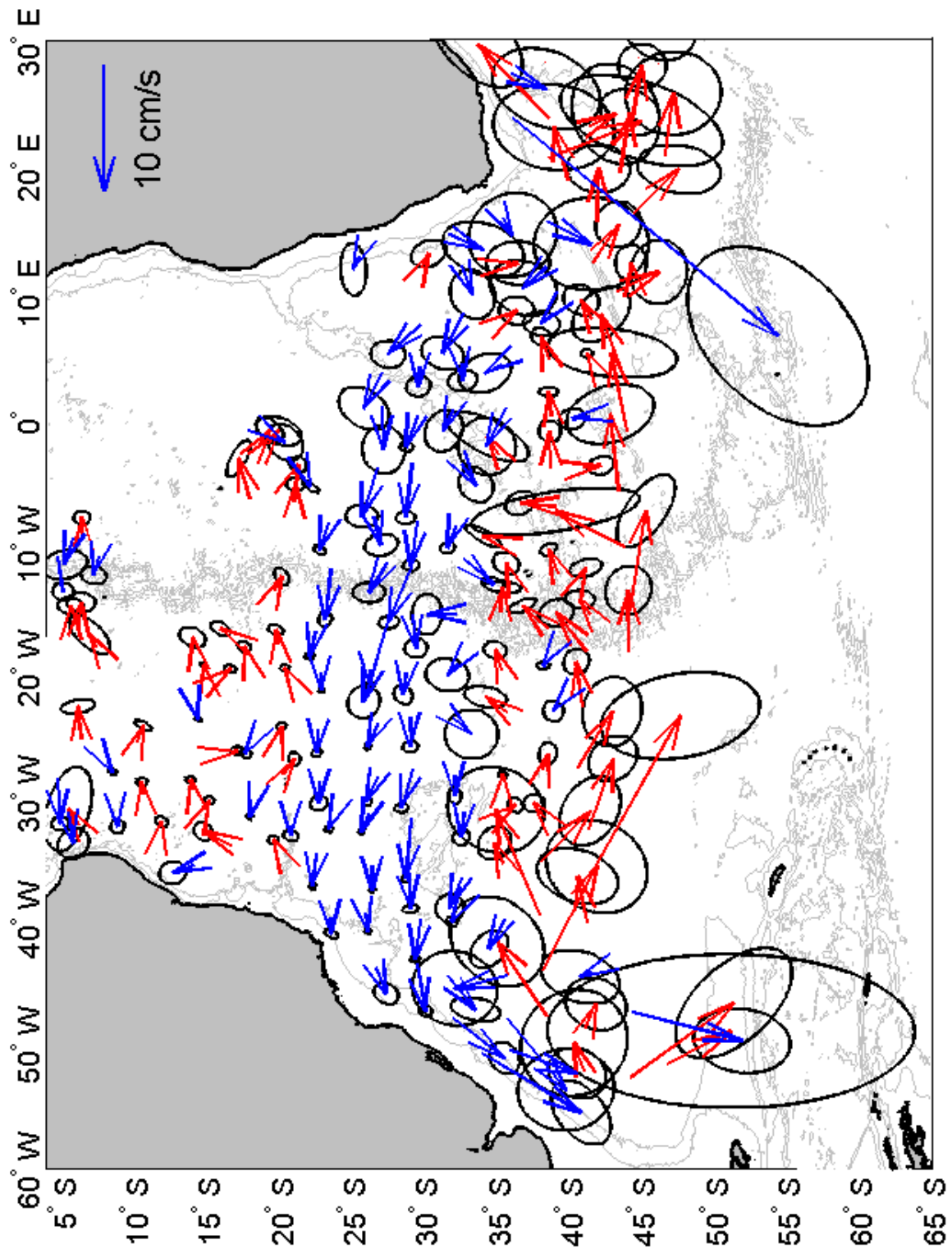


Figure 8. Average velocities for grid shown in Figure 7. The corresponding 63% probability error ellipses are shown centred on the tip of each velocity arrow.

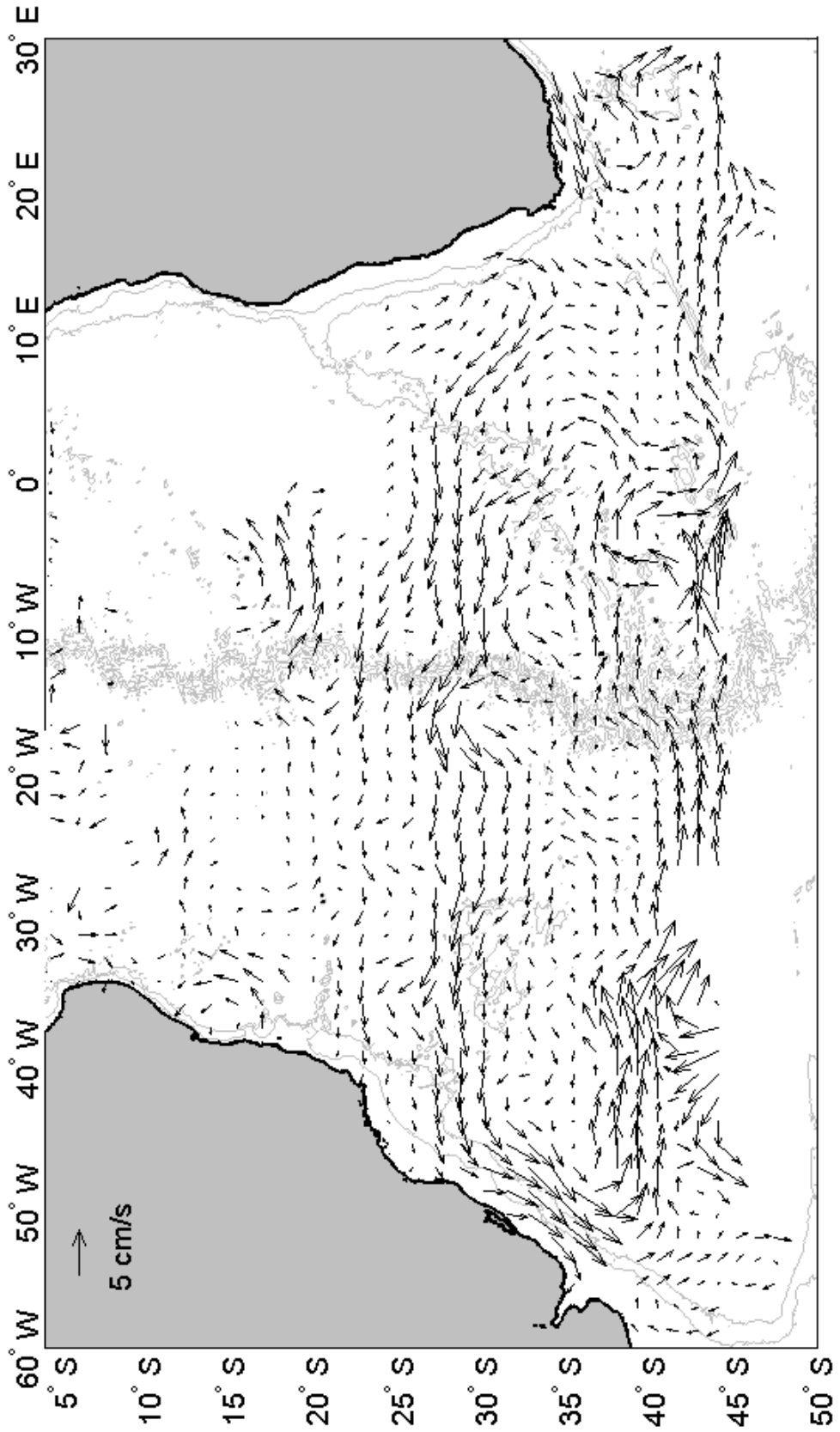


Figure 9. Objectively mapped velocities for float data shown in Figure 8.



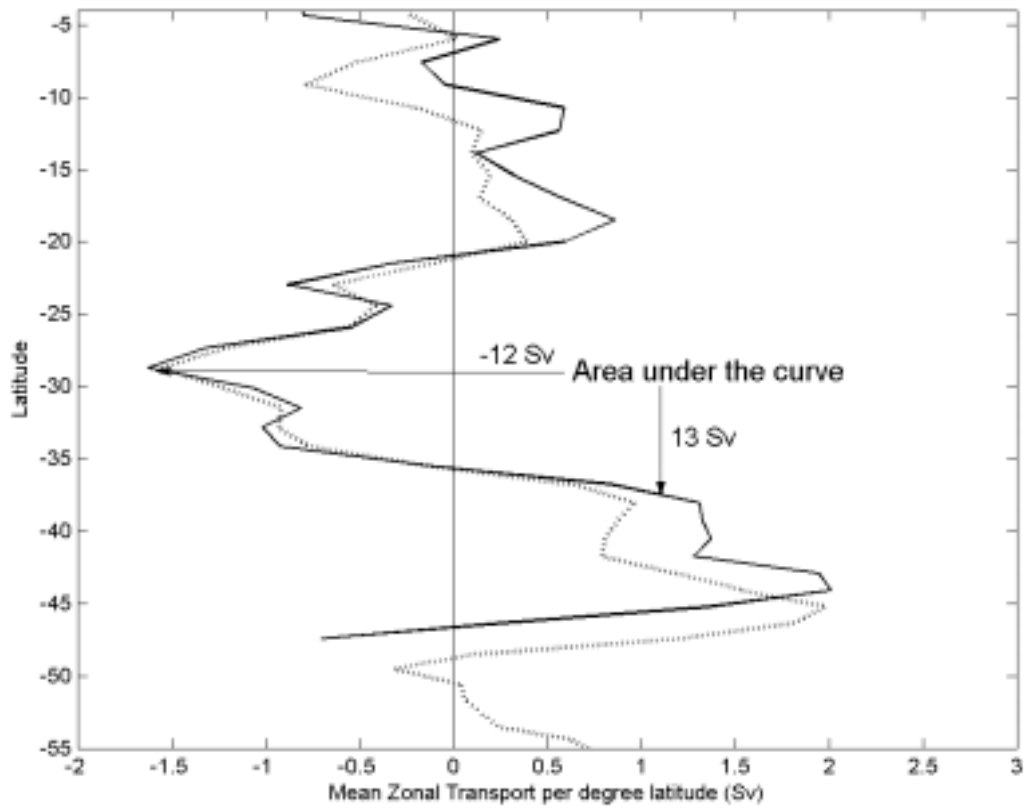


Figure 11. Lagrangian mean zonal transport across the entire basin. The continuous line is the layer transport as confined by neutral density surfaces, whereas the dotted line describes the layer transport confined by isobaric surfaces. Values are in Sv per degree latitude (positive east).

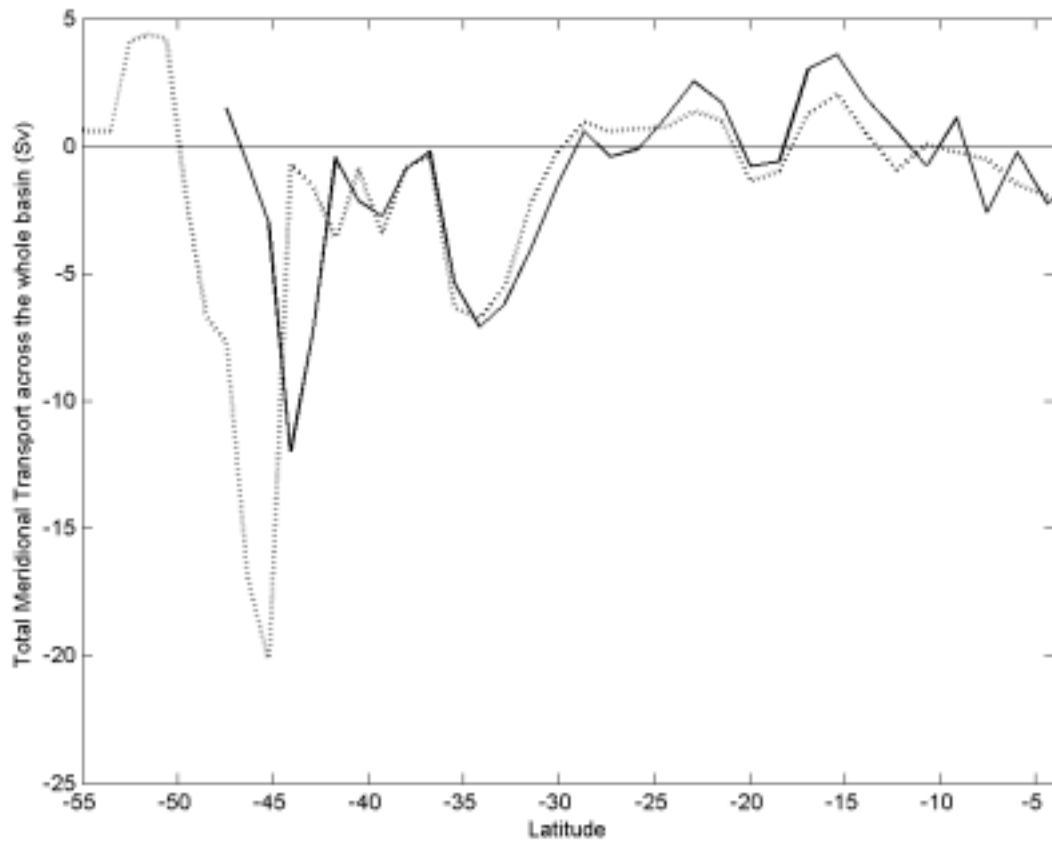


Figure 12. Comparison of Lagrangian meridional transports integrated across the entire basin from America to Africa. Line identification as in Figure 11.

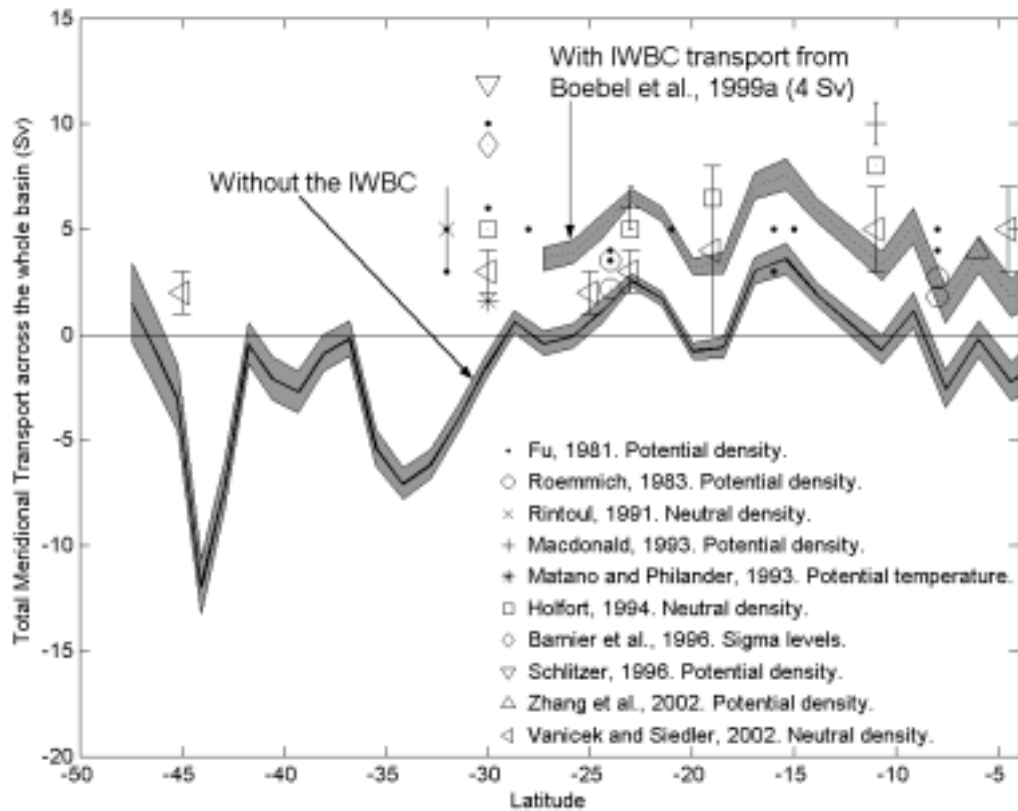


Figure 13. Comparison of Lagrangian meridional transports integrated across the entire basin with values found in the literature. Error bars (from the 68% confidence interval) are shown as a shaded area. Values are in Sv.

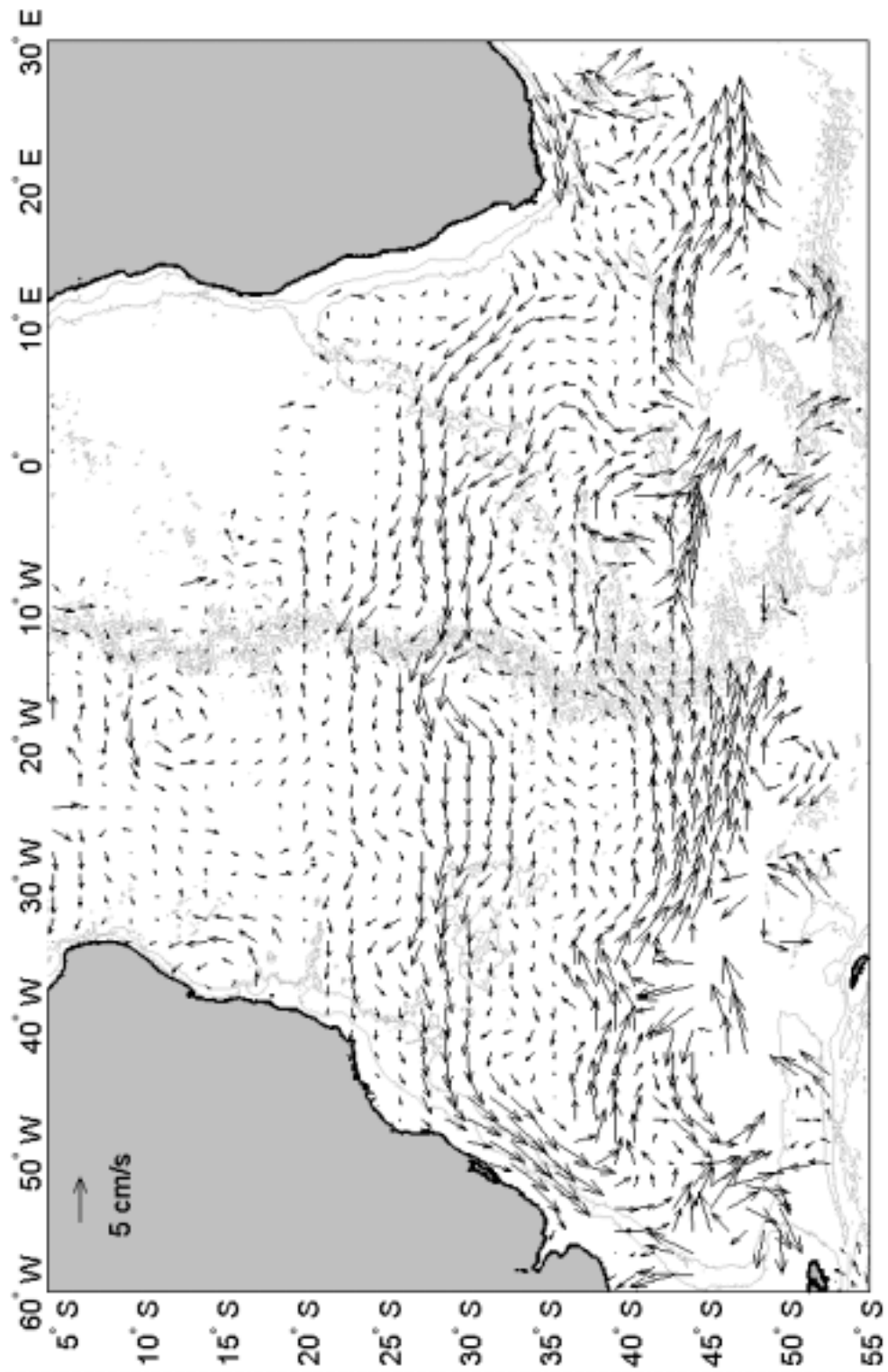


Figure 14. Objectively mapped velocities for float data confined by isobaric surfaces (650 and 1050 dbars)

## Figure Captions

Figure 1. Meridional section of salinity along approximately 25°W, from South Georgia Island to Iceland, from 1988-1989. The two curves passing through the AAIW are the 31.7 and 31.9  $\sigma_1$  isopycnal contours. Modified from Talley (1996, her Figure 1 (a)).

Figure 2. Schematics of AAIW circulation in the South Atlantic (adapted from You (2002)).

Figure 3. Float trajectory data without vertical selection. Most of the floats drifted between 400 and 1200 dbars with displacement periods of 10 days. For clarity, only descent positions are shown. Each of the six float programs is symbolized by a unique identifier, but high data density renders individual trajectories indistinguishable.

Figure 4. Hydrographic stations used in You, 2002, (his figure 2) to extract neutral density surfaces for AAIW.

Figure 5 Flow chart of float data processing. Data sets are denoted with ellipses and data processes with rectangles. As a reference in the text, for each process step there is a number in a circle.

Figure 6. Number of float-days for data confined by neutral surfaces.

Figure 7. Grid used for space-time average of the final results. Cells are based on an initial regular grid of 3° (latitude) x 4° (longitude) and deformed using Formula 1 with  $f/h$  and  $\mu = 6000$ .

Figure 8. Average velocities for grid shown in Figure 7. The corresponding 63% probability error ellipses are shown centred on the tip of each velocity arrow.

Figure 9. Objectively mapped velocities for float data shown in Figure 8. A reference arrow of 5 cm s<sup>-1</sup> is shown.

Figure 10. Stream function calculated from data shown in Figure 9. Contour values are in units of transport per depth (Sv km<sup>-1</sup>)

Figure 11. Lagrangian mean zonal transport across the entire basin. The continuous line is the layer transport as confined by neutral density surfaces, whereas the dotted line describes the layer transport confined by isobaric surfaces. Values are in Sv per degree latitude (positive east).

Figure 12. Comparison of Lagrangian meridional transports integrated across the entire basin from America to Africa. Line identification as in Figure 11. Values are in Sv (positive north).

Figure 13. Comparison of Lagrangian meridional transports integrated across the entire basin with values found in the literature. Error bars (from the 68% confidence interval) are shown as a shaded area. Values are in Sv.

Figure 14. Objectively mapped velocities for float data confined by isobaric surfaces (650 and 1050 dbars).

## Tables

**Table 1. Listing of float data by program.**

Name of the program	Number of floats	First transmission (m/y)		Last transmission (m/y)		Number of float years	Area in which the floats drifted (lat1-lat2, lon1-lon2)				References
AWI	38	3	2000	3	2003	27	-69	-48	-6	40	
Argo	60	8	1997	6	2003	62	-43	-4	-49	30	<a href="http://argo.jcommops.org/">http://argo.jcommops.org/</a>
WOCE/DBE	42	11	1994	1	1999	72	-61	-25	-68	40	Davis et al., 1996; Davis 1998
KAPEX	101	3	1997	9	1999	94	-50	-18	-31	40	Boebel et al., 2003a
WOCE	71	12	1992	10	1996	60	-45	-4	-56	-13	Zenk et al., 1998
SAMBA	74	2	1994	12	2001	136	-46	-4	-55	-4	Ollitrault et al., 1994a Ollitrault, 1995
$\Sigma$	386	12	1992	6	2003	451	-69	-4	-68	40	

**Table 2. Alignment numbers as calculated for various grid configurations. The first two columns describe the dimensions of the original rectangular cells before deformation. The third column indicates the corresponding  $\mu$  value. The next three columns specify the alignment number obtained for each of the grids as deformed following each of the physical variables: bathymetry, f/H and f/h. Minimum values for each variable and original grid size are marked in grey and overall minimum value (also for each original grid size) are emphasized by bold letters.**

Alignment Number .....						Alignment Number					
Lat	Lon	$\mu$	f/H	f/h	Bath	Lat	Lon	$\mu$	f/H	f/h	Bath
2	3	0	0,9417	0,9291	<b>0,7922</b>	4	5	0	0,9434	0,7989	<b>0,6271</b>
2	3	100	0,937	0,777	0,915	4	5	100	0,784	0,612	0,937
2	3	300	0,935	0,772	0,903	4	5	300	0,696	0,61	0,849
2	3	500	0,913	0,776	0,907	4	5	500	0,761	0,623	0,83
2	3	700	<b>0,902</b>	0,779	0,877	4	5	700	<b>0,797</b>	0,622	0,79
2	3	900	0,927	0,77	0,87	4	5	900	0,814	0,632	0,871
2	3	1100	0,931	-	0,858	4	5	1100	0,822	-	0,968
2	3	1500	-	0,755	-	4	5	1500	-	0,643	-
2	3	3000	-	0,785	-	4	5	3000	-	<b>0,586</b>	-
2	3	6000	-	<b>0,751</b>	-	4	5	6000	-	0,635	-
2	4	0	0,9385	0,8535	<b>0,7167</b>	4	8	0	0,7560	0,6216	<b>0,5644</b>
2	4	100	0,849	0,731	0,948	4	8	100	0,649	<b>0,53</b>	0,828
2	4	300	0,863	0,735	0,907	4	8	300	0,637	0,558	0,839
2	4	500	0,848	0,737	0,866	4	8	500	0,69	0,58	0,833
2	4	700	<b>0,832</b>	0,736	0,852	4	8	700	<b>0,627</b>	0,585	0,756
2	4	900	0,856	<b>0,729</b>	0,873	4	8	900	0,648	0,556	0,777
2	4	1100	0,826	0,732	0,87	4	8	1100	0,706	-	0,88
2	4	1500	-	0,742	-	4	8	1500	-	0,612	-
2	4	3000	-	0,742	-	4	8	3000	-	0,622	-
2	4	6000	-	-	-	4	8	6000	-	0,666	-
3	4	0	0,9307	0,8145	<b>0,7072</b>	5	5	0	0,8567	0,7462	<b>0,7396</b>
3	4	100	0,766	0,683	0,922	5	5	100	0,739	0,754	0,871
3	4	300	0,745	0,703	0,922	5	5	300	<b>0,697</b>	0,738	0,868
3	4	500	0,764	0,702	0,944	5	5	500	0,712	0,733	0,828
3	4	700	0,734	0,703	0,912	5	5	700	0,723	0,72	0,816
3	4	900	<b>0,71</b>	0,718	0,929	5	5	900	0,706	<b>0,705</b>	0,809
3	4	1100	0,714	-	0,908	5	5	1100	0,716	-	0,789
3	4	1500	-	0,686	-	5	5	1500	-	0,801	-
3	4	3000	-	0,671	-	5	5	3000	-	0,785	-
3	4	6000	-	<b>0,646</b>	-	5	5	6000	-	0,765	-
3	6	0	1,1094	0,9191	<b>0,7921</b>						
3	6	100	0,853	0,737	1,108						
3	6	300	0,906	0,754	1,116						
3	6	500	0,885	0,757	1,06						
3	6	700	0,866	0,745	1,038						

3	6	900	0,848	0,722	1,02
3	6	1100	0,833	-	1,013
3	6	1500	-	0,711	-
3	6	3000	-	0,58	-
3	6	6000	-	<b>0,551</b>	-

--	--	--	--	--	--

(Table 2: continued)

### Table Captions

Table 1. Listing of float data by program.

Table 2. Alignment numbers as calculated for various grid configurations. The first two columns describe the dimensions of the original rectangular cells before deformation. The third column indicates the corresponding  $\mu$  value. The next three columns specify the alignment number obtained for each of the grids as deformed following each of the physical variables: bathymetry,  $f/H$  and  $f/h$ . Minimum values for each variable and original grid size are marked in grey and overall minimum value (also for each original grid size) are emphasized by bold letters.